Original Research Article

Advancing Flexible Rope Motion Measurement in Aerospace: Vision-Based Innovations for Enhanced Accuracy and Efficiency through Edge Segmentation

 MohammadHassan Pachenari[1]*

1- Department of Mechanical Engineering, Central Tehran Branch, Islamic Azad University, Tehran, Iran

ABSTRACT

Flexible ropes have wide-ranging applications in aerospace engineering, yet accurately measuring their motion state without disrupting dynamic characteristics remains a challenge. This study introduces a visual measurement method aimed at precisely assessing flexible rope motion to support the development and validation of an accurate cable dynamics model. Addressing non-uniform movement speeds attributed to the rope's large length-diameter ratio, a novel tether edge segmentation operator is proposed to delineate motion blur regions into exposure beginning and ending time tethers. This operator enhances accuracy over existing centerline extraction methods, particularly in asymmetric motion blur regions. The proposed approach not only resolves accuracy issues during high-speed motion but also leverages the camera's inherent image acquisition frame rate, reducing system complexity and cost. Validation of the material point tracking algorithm through mathematical and physical simulations underscores its effectiveness in monitoring any point on the tether. Furthermore, verifying the tether dynamics model through the absolute nodal coordinate method highlights the novelty and significance of this research in advancing aerospace engineering applications

Introduction

In recent years, the rapid development of space technology has catalyzed the diversification and heightened complexity of space missions, ushering in a new era of innovation and exploration. This evolution has sparked the emergence of a diverse array of flexible spacecraft, characterized by utilizing space rope systems as primary structural elements. These spacecraft are multifaceted, engaging in tasks ranging from rope satellite formation [1,2], and electrodynamic rope deorbiting [3,4], to the intricate maneuvering involved in capturing space nets [5,6]. The incorporation of space ropes holds immense promise, owing to their intrinsic qualities of lightweight construction, low damping properties, exceptionally high tensile strength, and remarkable flexibility, rendering them uniquely suited for a myriad of spaceborne endeavors.

In the unique microgravity environment, cable structures manifest complex dynamic behaviors, exhibiting transverse and longitudinal vibrations, along with the phenomenon of rope-skipping movements. Such intricate dynamics come into play during crucial phases of space missions, including expansion, state maintenance, and recovery [7]. Therefore, validating the accuracy of cable dynamic models through physical experimentation becomes paramount. Conventional modeling methodologies, which hinge upon assumptions of small deformation and rotation, confront inherent limitations when applied to the analysis of flexible ropes characterized by their substantial scale, low stiffness, and pronounced deformations. Enter the absolute node coordinate method [8,9], heralded as

1(Corresponding Author), Mohammad Hassen Pachenari, Assistant Professor, Email: moh.pachenari@iauctb.ac.ir

a breakthrough in the realm of large deformation flexible precision dynamics modeling.

The central aim of this paper is to undertake comprehensive dynamic modeling of cable-beam elements, leveraging the absolute node coordinate method as the cornerstone, with a deliberate emphasis on conducting numerical simulations [10-17] to underscore the validity and efficacy of the ANCF method, juxtaposed against real-world experiments. To achieve precise dynamics measurements, an arsenal of techniques, including force sensors and resistance strain gauges, has been enlisted [18-20]. For instance, Sauter [19] employed strain gauge sensors to gauge torque at the fixed terminus of the rope meticulously.

While traditional contact measurement techniques afford reliability in capturing data pertaining to minor deformations, they prove inadequate in the face of the considerable deformations and expansive motion ranges characteristic of cables. Vision-based measurement methodologies, conversely, offer a panoply of advantages, including non-contact operation, expansive measurement fields, and minimal environmental requisites. Pioneering endeavors, such as Irvine's [21] monocular vision measurements of vibratory ropes, albeit commendable, fell short in accurately quantifying rope motion velocity and displacement. Subsequent studies by Anguilla [22], Yoo [23-25], Jung [26], and Kawaguti [27] have pushed the envelope, employing vision-based techniques to measure the motion of flexible structures with increasing precision.

Nevertheless, challenges persist, particularly in mitigating the influence of external markers on rope motion. Domae [31] proposed the innovative use of lasers for rope marking, while Liu [32,33] devised a centerline match method predicated on binocular vision, obviating the need for physical markers. Additionally, E [34] introduced a versatile material point tracking algorithm adept at accommodating cable bending and longitudinal elastic deformation, thereby enabling the tracking of cable points sans supplementary features.

Despite notable advancements, the specter of motion blur looms large, casting a shadow on the accuracy of image-based rope tracking methodologies. To surmount this challenge, a novel rope edge segmentation operator has been conceived, designed to delineate motion blur regions, thereby enhancing accuracy under high-speed motion scenarios, elevating image acquisition frame rates, and concurrently streamlining system complexity and cost.

Expanding on the significance of this research, it is crucial to underscore the pivotal role that accurate dynamic modeling and measurement techniques play in advancing the field of space technology. With the increasing complexity and diversity of space missions, the demand for robust methodologies capable of accurately capturing and analyzing the dynamics of flexible structures like space ropes has never been greater. By addressing the limitations of traditional modeling approaches and measurement methods, this research not only contributes to the theoretical understanding of cable dynamics but also has practical implications for the design, operation, and maintenance of flexible spacecraft.

Furthermore, the findings of this study have broader implications beyond the realm of space exploration. The methodologies and techniques developed herein can be applied to a wide range of engineering disciplines, including robotics, structural engineering, and aerospace engineering. The ability to accurately model and measure the dynamics of flexible structures is invaluable in fields where lightweight, high-strength materials are employed, such as in the design of unmanned aerial vehicles, offshore structures, and medical devices.

In addition to its practical applications, this research contributes to the theoretical foundations of dynamics and control theory. The development of novel modeling methodologies, such as the absolute node coordinate method, expands the toolkit available to researchers and engineers, enabling them to tackle increasingly complex problems in the realm of flexible structures and dynamics. By pushing the boundaries of current knowledge and exploring new avenues of research, this study paves the way for future advancements in the field of dynamics and control.

In conclusion, the rapid development of space technology has opened up new frontiers of exploration and innovation, ushering in an era of unprecedented complexity and diversity in space missions. Flexible structures, such as space ropes, play a pivotal role in enabling these missions, offering lightweight, high-strength solutions to the challenges of space exploration. By developing novel modeling and measurement techniques, this research contributes to our understanding of the

dynamics of flexible structures and lays the groundwork for future advancements in space technology and beyond.

Figure 1. Rope image of free-falling from the horizontal.

Image extraction based on rope motion blur

Definition of pixel points at the rope edge of the motion blur region

Edge detection is performed on the rope image. The Canny edge detection operator is used to obtain the edge image of the rope, as shown in Figure 1. The edge image of the rope is a closed single-pixel area, which includes the movement state of the rope at the beginning and end of the exposure, As can be seen in the figure, the movement track of the rope is fixed at the endpoint. When the rope moves around the axis or straight line, the edge pixel of the rope will be mutated at the start and endpoints of the rope. With the correct segmentation point on the edge of the rope, the edge image of the fuzzy region can be divided into two parts; therefore, the image coordinates of the rope at the initial and end of exposure can be obtained .

The edge of the rope discussed in this paper is a close area with a single pixel. There are three types of pixels, defined as smooth point, knot, and segment point .

1. *Smooth Point*: If the point is in line with its adjacent points (for any point on edge), this point would be called a smooth point, and an extension in the pixel direction of such a point does not change.

2. *Knot Point*: If the point is not aligned with its adjacent points (for any point on edge), this point would be called knot point and an extension in the pixel direction of such a point can be changed.

3. *Segment Point*: The point on edge can be divided into three parts, part one is rope configuration at the initial of exposure time and part two is rope configuration at the end of exposure time as well as the track of the end tip point Is part three.
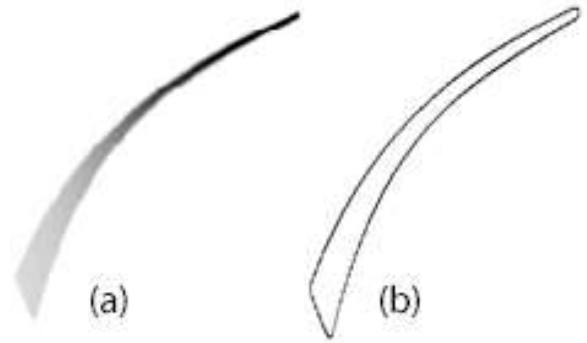
Figure 2. Motion blur image and edge detection result image of rope:(a) Motion blur image;(b) Edge detection result.

In this paper, a rope motion-blurred segmentation operator is designed that marks the pixel points whose slope changes on the edge of the rope. This operator is a 3×3 anti-centrosymmetric matrix, which denoted as

$$O_{ces} = \begin{bmatrix} o_{11} & o_{12} & o_{13} \\ o_{21} & 0 & -o_{21} \\ -o_{13} & -o_{12} & -o_{11} \end{bmatrix} \quad (1)$$

When the operator center point moves along the rope edge line in the order of the Freeman chain code, the pixel point after the convolution operation with the surrounding pixel can be written as a vector:

$$\hat{p} = [u, v, \tau]^T \quad (2)$$

Where u,v is the image coordinate of the edge of the rope, τ is the operation result of the pixel and edge segmentation operator.

When the edge of the rope is a smooth point the slope of the smooth point does not change and $\tau = 0$ and when the edge of the rope is a node, the slope of the node changes and $\tau \neq 0$. Moreover, the value of τ is unique for different connections. As features of each pixel, smooth points and knots can be quickly identified as these values. At the same time, the connection mode with dual values has the characteristic that the rope is locally bent but still extends in the previous direction. With this characteristic, the segmentation points can be screened out from the knots. The elements O_{ces} can be determined as follows:

$$\begin{cases} -o_{11} - o_{13} = \tau_1 \\ o_{11} - o_{21} = \tau_2 \\ -o_{13} - o_{21} = \tau_3 \\ o_{12} - o_{13} = \tau_4 \\ -o_{11} + o_{13} = \tau_5 \\ -o_{11} + o_{12} = \tau_6 \end{cases} \quad (3)$$

Where $\tau_1 \neq \tau_2 \neq \tau_3 \neq \tau_4 \neq \tau_5 \neq \tau_6, \tau_i \in N^*$, written in the matrix:

$$Bo = A \qquad (4)$$

Where $o = [o_{11} \quad o_{12} \quad o_{13} \quad o_{21}]^T$;
$A = [\tau_1 \quad \tau_2 \quad \tau_3 \quad \tau_4 \quad \tau_5 \quad \tau_6]^T$,

$$B = \begin{bmatrix} -1 & 0 & -1 & 0 \\ 1 & -1 & 0 & 0 \\ 0 & 0 & -1 & -1 \\ 0 & 1 & -1 & 0 \\ -1 & 0 & 1 & 0 \\ -1 & 1 & 0 & 0 \end{bmatrix} \qquad (5)$$

Solving the equation using the least squares method, we can get

$$o = (B^T B)^{-1} BA, \qquad (6)$$

Taking a set of mutually different positive integers as elements of A, we can obtain a set of o as the elements of the edge segmentation operator, so the edge segmentation operator is not unique. In this paper, the value of one set of such matrices is given:

$$O_{ces} = \begin{bmatrix} -3 & 6 & 2 \\ -5 & 0 & 5 \\ -2 & -6 & 3 \end{bmatrix}, \qquad (7)$$

The values of τ with different connection modes are shown after calculating the segmentation operator and the edge line of the rope according to the above values :
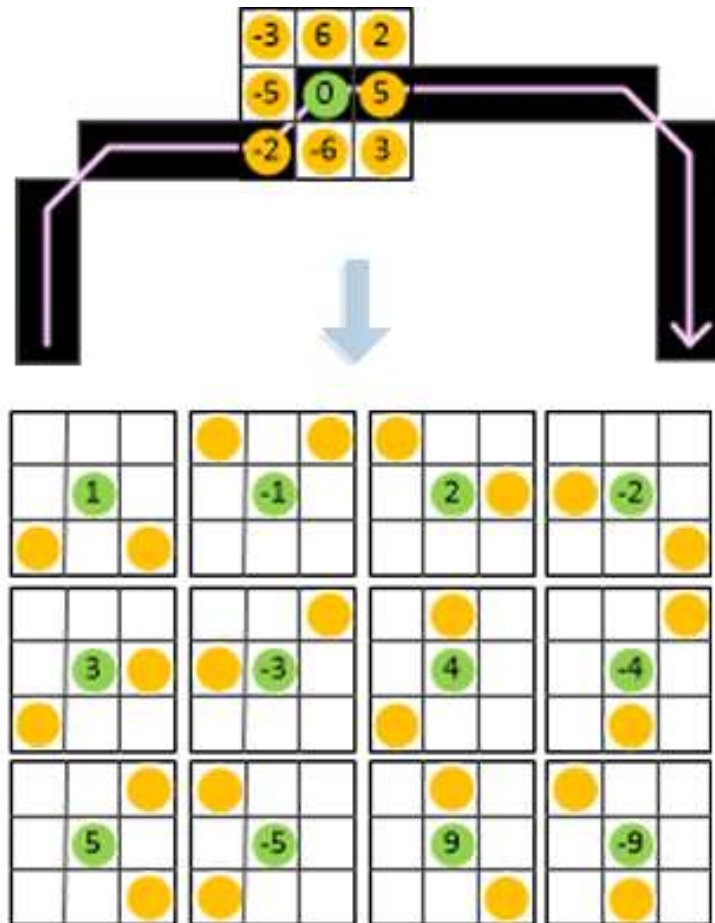

Figure 3. The result of the segment operator operating on the image edge pixel

Segmentation feature description

With the segmentation operation, the set of pixel points $\{\hat{p}_j\}, j = 1,2,\cdots,m$ can be denoted as $\{\hat{p}_i\}, i = 1,2,\cdots,n$ after removing the smooth points $\tau_j = 0$. The point set $\{\hat{p}_i\}$ is composed of knots, and the slope of the edge line of the rope changes at the knot. However, the edge is the pixel width, and the image coordinates are integer discrete values, so the angle of the direction can take only two degrees, 90° and 120°. In addition, at the segmentation point, angle changes may

occur due to factors such as the curvature of the rope or noise. Therefore, it is necessary to analyze the difference between the segmentation point and other knots in order to accurately select the segmentation point from among the knots.

Feature 1: Select the segmentation point according to the central symmetry of the motion blur segmentation operator

The rope undergoes changes in the tangential direction when its curvature changes. Due to the relatively large diameter of the rope, there is no significant change in the radial direction. Therefore, we can identify candidate segments by utilizing the central symmetry of the motion blur edge segmentation operator. The rules are as follows:

(1.1). When $\tau_i + \tau_{i+1} \neq 0 \& \tau_i + \tau_{i-1} \neq 0$ $\hat{p}_i$ is the segmentation point;

(1.2). When $\tau_i + \tau_{i+1} = 0 \& \tau_i + \tau_{i-1} = 0$ $\hat{p}_i$ is the knot;

(1.3). When $\tau_i + \tau_{i+1} \neq 0 \& \tau_i + \tau_{i-1} \neq 0$ extending the range of detection:

(1.3.1). When $\tau_{i-1} + \tau_{i+2} = 0 || \tau_{i+1} + \tau_{i-2} = 0$ $\hat{p}_i$ is the knot;

(1.3.2). Otherwise $\hat{p}_i$ is the segmentation point. Where,

$$\tau_{i-1} = \begin{cases} \tau_{i-1} & i = 2, \cdots, n \\ \tau_n & i = 1 \end{cases}$$
$$\tau_{i+1} = \begin{cases} \tau_{i+1} & i = 1, \cdots, n+1 \\ \tau_1 & i = n \end{cases}$$
$$\tau_{i-2} = \begin{cases} \tau_{i-2} & i = 3, \cdots, n \\ \tau_n & i = 2 \\ \tau_{n-1} & i = 1 \end{cases} \quad (8)$$
$$\tau_{i+2} = \begin{cases} \tau_{i+2} & i = 1, \cdots, n-2 \\ \tau_1 & i = n-1 \\ \tau_2 & i = n \end{cases}$$

Feature 2: Select a knot with an angle of 90° as the segmentation point Tables

When the knot is on the edge line of the rope $\tau_i \in \{\pm 1, \pm 5\}$, the angle of the point is 90°. With respect to the angle of 120°, the direction of the edge line of the rope at the knot changes drastically, and the knot should be regarded as a candidate segmentation point. With the influence of noise, a burr is generated on the edge line, which is usually $\tau_i \in \{\pm 1, \pm 5\}$. Thus, in this case, it is necessary to further detect τ_{i-1} and τ_{i+1}, and calculate whether the angle between the two knots is less than 120°. In addition, two adjacent knots can also form an angle of 90°. The rules are as follows:

(2.1). When $\tau_i \in \{\pm 1, \pm 5\}$ the detection range should be extended from the point $\hat{p}_{i-2}$ to $\hat{p}_{i+2}$. Besides, $r_1 = [u_i - u_{i-2} \quad v_i - v_{i-2}]^T$, $r_2 = [u_i - u_{i+2} \quad v_i - v_{i+2}]^T$ and the angle between the two vectors is $\theta = arccos\left(\frac{r_1 r_2}{\|r_1\|\|r_2\|}\right)$ should be calculated.

(2.1.1). When $\theta \geq 120°, \hat{p}_i$ is the knot generated by noise;

(2.1.2). When $\theta < 120°, \hat{p}_i$ is the segmentation point;

Figure 4. Extending the detection range to calculate θ in the condition of (2.1)

(2.2). When $(\boldsymbol{\tau_i, \tau_{i+1}}) \in \{(\mathbf{3, -4}), (\mathbf{-3, 4}), (\mathbf{-2, -9}), (\mathbf{2, 9})\}, \hat{\boldsymbol{p}}_i$ is the segmentation point

Feature 3: Select the knot in the end regions of the rope as the segmentation point

Although the centerline extraction algorithm has lower accuracy for extracting motion-blurred images, the position of the endpoints at the centerline can be used to constrain the range of the segmentation points. Set the endpoints of the centerline are $\hat{p}_{e1}$ and $\hat{p}_{e2}$, the segmentation point should be located near the point $\hat{p}_{e1}$ and $\hat{p}_{e2}$.

"The distances from each knot to the two endpoints are defined as follows:

$$r_{e1} = [u_i - u_{e1} \quad v_i - v_{e1}]^T$$
$$r_{e2} = [u_i - u_{e2} \quad v_i - v_{e2}]^T$$

In this formulation, u_i and v_i represent the coordinates of the knot, u_{e1} and v_{e1} represent the coordinates of endpoint 1, and u_{e2} and v_{e2} represent the coordinates of endpoint 2.

The points within the threshold range are the candidate segments.

(3.1). When $\|r_{e1}\| < T \cup \|r_{e2}\| < T$, $\hat{p}_i$ is the segmentation point;

(3.2). When $\|r_{e1}\| \geq T \cap \|r_{e2}\| \geq T$, $\hat{p}_i$ is the knot.

True segmentation point screening rules

On the basis of the feature description in the above section, all knots are computed with the feature and a scoring mechanism is established for each feature. Finally, the point with the highest score is the segmentation point.

According to the scoring rules defined in Table 1, the final score of each knot on the edge of the rope

can be divided into five levels, 2.5, 2, 1.5, 1, 0.5, and 0, in which the first two grades serve as the candidate points for segmentation and the last three grades only serve as common knots. Knots with different score levels are marked with different colors, as shown in Fig. 4. The red marker points are knots with a score of 2.5, the green points are knots with a score of 2, and the yellow points are knots with a score of 1.5. The red and green knots are located near the segmentation point of the rope edge, the yellow knots are far from the true segmentation point, and the other knots with lower scores are not located near the segmentation point of the rope edge.

**Table 1**. Score table of segment point candidates

Feature			Score
Feature one	(1.1)		1
	(1.2)		0
	(1.3)	(1.3.1)	0
		(1.3.2)	0.5
Feature Two	(2.1)	(2.1.1)	0
		(2.1.2)	0.5
	(2.2)		0.5
Feature three	(3.1)		1
	(3.2)		0

As can be seen from Figure 4, multiple candidate segmentation points are near the same segmentation point, and it is necessary to cluster the candidate points belonging to the same segmentation point to retain one. In this study, the real rope edge segmentation point can be selected according to the candidate segmentation screening process, as shown in Figure 5.

Figure 5. Segment point candidate on the flexible rope with a different score

This study compares this method, as shown in Figure 6, with the Harris corner extraction method.
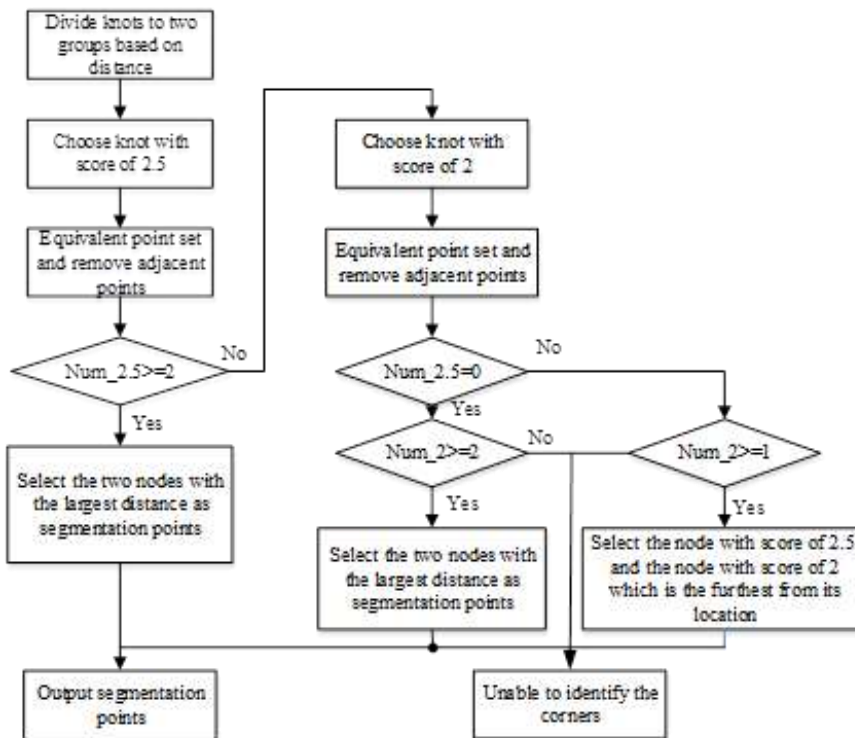
Figure 6. Flow chart of segment point candidate selection

In Figure 7, Parts a and b are the edges of the rope images at the same time. Part a is the segmentation point detected by the algorithm used in this research, and Part b is the segmentation point

detected by Harris. Parts c d are the rope edge images at another time and are similar.

It can be seen that numerous knots have been detected by the Harris corner, while the algorithm in this paper can correctly detect segmentation points and screen out knots at the same time. The effectiveness of the motion blur segmentation algorithm proposed in this study is verified by comparing the detection results with the Harris corner extraction method.
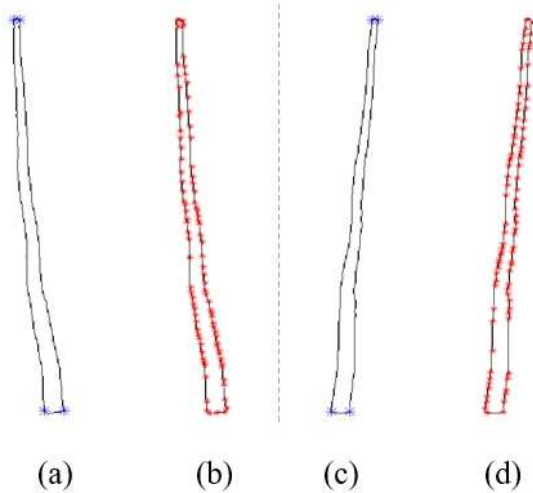
Figure 7. Comparison between edge segment operator detection results and the Harris corner method

Measuring rope motion state based on material point tracking

The material point tracking algorithm in reference [34] is used to track any point on the flexible rope. The length of the cable is constant regardless of the effects of force, and without considering plastic deformation, the distance between each point on the cable and its starting point is constant. According to this principle, the motion state of any point on the rope can be tracked by judging its length. When elastic deformation is considered, the length of the cable is elongated or shortened during motion. Assuming that the variation of this length is uniform on the cable unit, when the entire cable is stretched from Lc0 to Lc, the distance from the cable end will change from l to l(Lc/Lc0), as shown in Figure 8.

The algorithm flow of rope material point tracking is as follows:

1. The knots on the cable sequence at each moment were extracted by the motion blur segmentation operator, and these knots were arranged in order from the beginning to the endpoint of the cable.

The cable point plane coordinates are represented as a point set $\{p_{ci}\}$, i = 1, 2, ..., n, and set the length of the tracking point from the cable end as l;

2. Using equation (9), all the distances among points in the setpoint $\{p_{ci}\}$ is accumulated to solve the length of the cable L_c, and the length of the cable without elastic deformation is L_{c0}. Therefore, the distance between the tracked point and the end of the cable is $l' = l\left(\frac{L_c}{L_{c0}}\right)$.
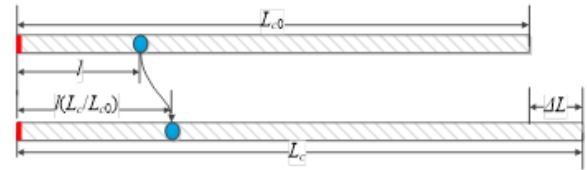
Figure 8. Cable element corresponding to elastic deformation

$$L_c = \sum_{i=1}^{n-1} \left\| \boldsymbol{P_{c(i+1)}} - \boldsymbol{P_{ci}} \right\|_2 \tag{9}$$

3. The set of points { p_{ci} } accumulates from the first point to point j, so that

$$l_j = \sum_{i=1}^{j-1} \left\| \boldsymbol{p}_{c(i+1)} - \boldsymbol{p}_{ci} \right\|_2 \leq l', j < n \tag{10}$$

For point j+1,

$$l_{j+1} = \sum_{i=1}^{j} \left\| \boldsymbol{p}_{c(i+1)} - \boldsymbol{p}_{ci} \right\|_2 > l', j+1 < n \tag{11}$$

The point tracked is between p_{cj} and $p_{c(j+1)}$;

4. Calculate the plane coordinate position of the tracked point p_t by equation (12).

$$\boldsymbol{p}_t = \boldsymbol{p}_{cj} + \frac{l' - l_j}{\left\| \boldsymbol{p}_{c(j+1)} - \boldsymbol{p}_{cj} \right\|_2} \left(\boldsymbol{p}_{c(j+1)} - \boldsymbol{p}_{cj} \right) \tag{12}$$

The above algorithm can obtain the motion state, and it is possible to track the point at any time when the cable length is l at the initial state

5. An experiment of motion state measurement for cable structure

5.1. Mathematical simulation experiment

In this test, the simulation image generated by the dynamic model of the cable, based on absolute nodal coordinates, is processed through mathematical simulation. The object being measured is a rope with the following general specifications:

Table 2. The properties of the rope.

specific	value
Length	1 m
Diameter	1 mm
Elastic modulus	1.24×10^{11} Pa
Passion's ratio	0.3
Aerodynamic Drag Factor	1.122

The parameter of the camera model is

$$M_{ins} = \begin{bmatrix} 1200 & 0 & 400 \\ 0 & 1200 & 256 \\ 0 & 0 & 1 \end{bmatrix} \quad (13)$$

The image size is 800×512 pixels, and the frame frequency is 30 FPS. For the plane coordinate system for rope movement, the x-axis is along the horizontal direction and the y-axis is along the direction of gravity. In this experiment, one end of the rope is fixed at the origin of the plane coordinate system and is released from the horizontal direction. The simulation image was generated to analyze the accuracy of rope image extraction and the material point tracking algorithm.

First, the centerline extraction algorithm is used to extract the image during the process of rope motion. Because the point performs non-uniform motion on the whole rope, the extraction accuracy of the rope center line will decrease with increasing exposure time. The image extraction error at the endpoint of the rope at different exposure times was analyzed, as shown in **Error! Reference source not found.**. The extraction error at the endpoint of the rope increases as the exposure time increases; however, when the rope moves at a higher speed, the image extraction error at the endpoint increases sharply with the increase in exposure time. The two peaks in the figure correspond to the two moments with the maximum speed.
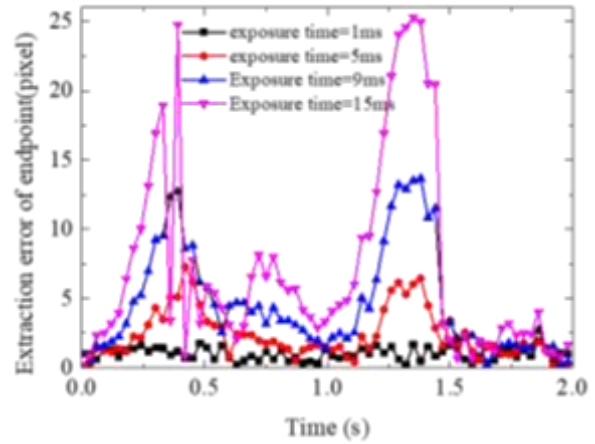
Figure 9. Image extraction accuracy of the rope endpoints at different exposure time.

Error! Reference source not found. shows the extraction results of the centerline at different peak times in **Error! Reference source not found.**. It can be seen that with an increase in exposure time, the end of the rope will generate a motion blur region, which is not symmetrical along the centerline direction. Therefore, the end region in the centerline extraction will be biased toward the direction with a larger gradient. This effect is more focused in parts d and h from Figure 10; it has fitted centerline extraction in short exposures because the rope is symmetrical along the centerline, as shown in parts a and e.
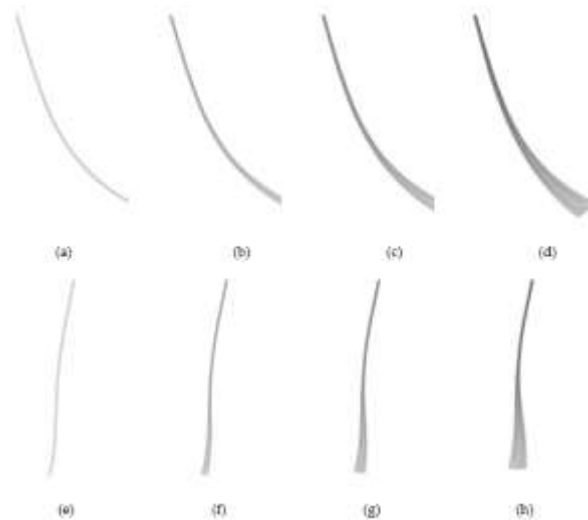
Figure 10. Extraction results of rope centerline at a different exposure time: (a) 1 ms exposure time;(b) 5 ms exposure time;(c) 9 ms exposure time;(d) 15 ms exposure time;(e) 1 ms exposure time;(f) 5 ms exposure time;(g) 9 ms exposure time;(h) 15 ms exposure time.
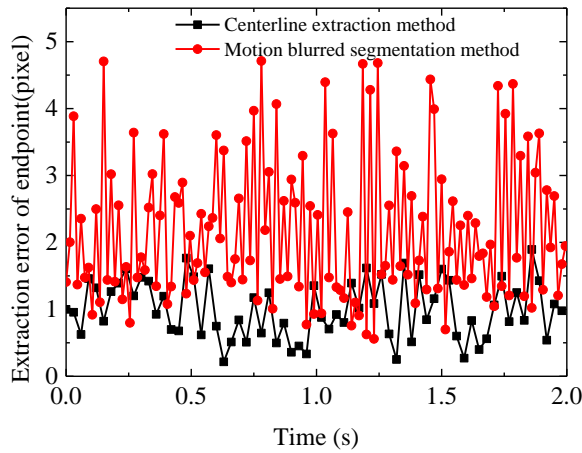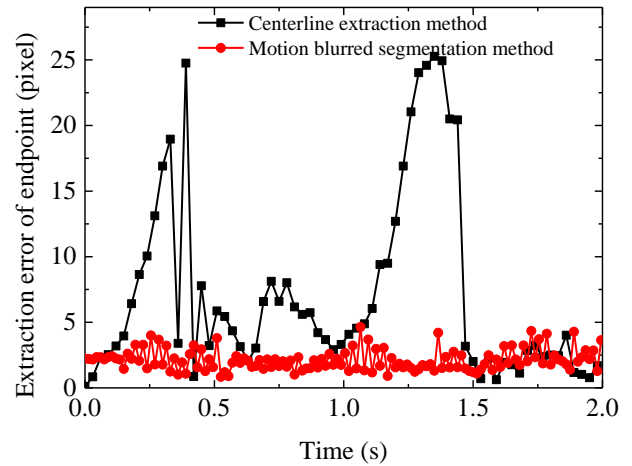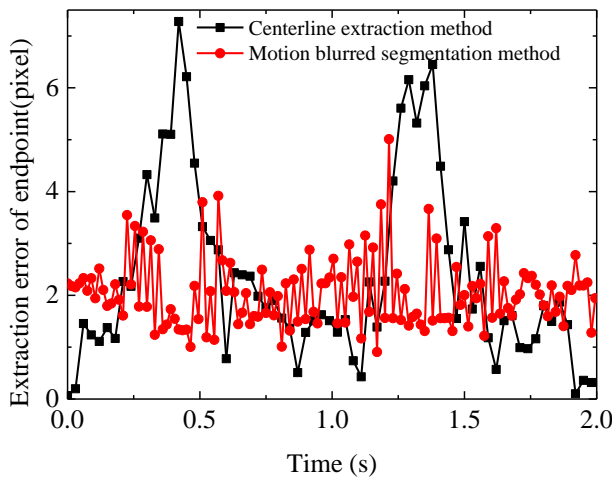
Figure 11.(a)
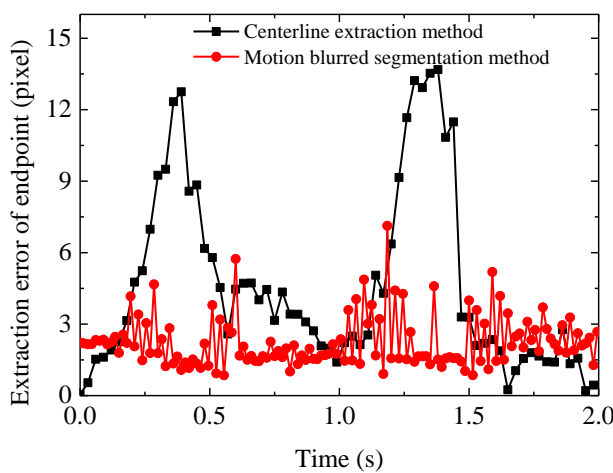

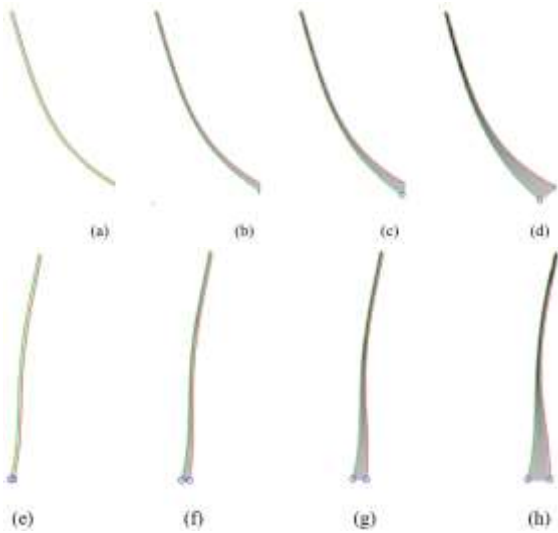**Figure 11.**(b)

Figure 11.(c)

Figure 11.(d)

Figure 1. Image extraction accuracy of two methods at different exposure times: (a) 1 ms exposure time; (b) 5 ms exposure time; (c) 9 ms exposure time; (d) 15 ms exposure time; (e).

To improve the accuracy of image extraction, the motion blur segmentation algorithm proposed in this paper is used to extract the rope image. Figure 11 compares and analyzes the extraction accuracy of the centerline extraction method and the motion blur segmentation algorithm at the endpoint of the rope. It can be seen that the centerline extraction method is superior to the motion-blurred image segmentation algorithm when the exposure time is short, but when the exposure time increases; the extraction accuracy of the motion-blurred image segmentation algorithm is better than that of the centerline extraction method. However, the accuracy of the motion-blurred image segmentation algorithm in some time periods is low. These periods correspond to the phase with a lower rope motion speed. In the phase with higher rope motion speed, the motion blur segmentation algorithm has more significant accuracy than the centerline extraction algorithm

Figure 12. Extraction results of rope at different exposure times by motion blur segmentation: (a) 1 ms exposure time;(b) 5 ms exposure time;(c) 9 ms exposure time;(d) 15 ms exposure time;(e) 1 ms exposure time;(f) 5 ms exposure time;(g) 9 ms exposure time;(h) 15 ms exposure time.

Physical simulation experiment

Experimental platform and vision measurement system errors

In this experiment, the rope is measured using a visual measurement method, and the errors of the visual measurement system and image extraction are analyzed, The measurement results are compared with the cable dynamic model based on the absolute node coordinate method to analyze the accuracy of the cable dynamic model. Since the rope movement has a higher speed, the image acquisition frequency is set as 119FPS, the image size is 544×1024 pixels, and the exposure time is 4 ms. For those tests, the camera needs to be recalibrated because the focal length and image size are adjusted.

The calibrated camera's internal parameter matrix is:

$$\begin{bmatrix} 1495.2341 & 0 & 508.0598 \\ 0 & 1483.2726 & 275.6076 \\ 0 & 0 & 1 \end{bmatrix} \quad (14)$$

The second-order radial distortion parameter is -0.1793, and the fourth-order radial distortion is 0.3891. The measuring object was a kevlar fiber rope with a length of 411 mm and a diameter of 1 mm. One end of the rope is fixed at a position 17 mm away from the background plane, and the other end is free and released by the horizontal position. The rope moves within the range of the black background plate, and the distance between the camera and the measuring plane is 1.5 m, as shown in Figure 13.

The extrinsic parameter matrix of the camera and the rope-moving plane $[R|t]$ is calculated using the checkerboard characteristic corners with known spatial coordinates on the measuring plane, and the coordinate system is established on the measuring plane, as shown in **Error! Reference source not found.**. The X-axis in the measurement plane coordinate system is along the horizontal direction, and the Y-axis is along the gravity direction. The origin of the coordinate system established by the checkerboard feature points is located at the upper left of the checkerboard. To facilitate the description of the movement of the rope, the checkpoint origin of the checkerboard feature points is translated to the fixed end of the rope.

Figure 13. The experiment with the equipment for flexible rope visual measurement.
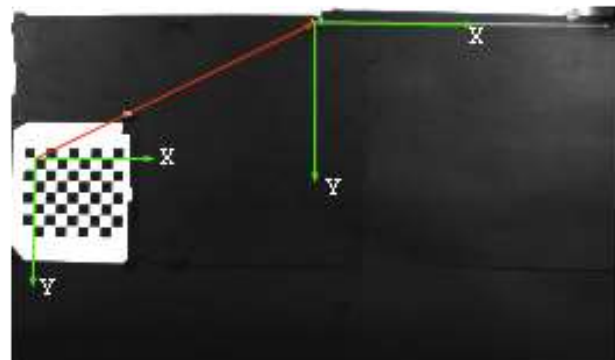

Figure 14. Coordination system of the measurement plane

The error of visual measurement is divided into two parts, one part is the extrinsic parameter matrix $[R|t]$ calculated by checkerboard feature corner points, and the other part is the rope image extraction algorithm. The error generated by the

extrinsic parameter matrix $[R|t]$ will be analyzed in this section, and the error generated by the image extraction algorithm will be analyzed in the following section. In the experiment, the spatial position of the feature corners in the checkerboard is known, and the image coordinates of the feature corners can be extracted from the image so that the extrinsic parameter matrix can be calculated by visual measurement.

In this test, the checkerboard provided 56 characteristic corners, and the image extraction coordinates of the feature corners caused errors. Meanwhile, the optimal solution is obtained in the process of solving the nonlinear equation, so there will be errors in the calculated extrinsic parameter matrix. To calculate the error caused by calculating the extrinsic parameter matrix, the spatial coordinates of the feature points are re-projected onto the image plane according to the calculated outer parameter matrix, and the image error of each feature point after re-projection is calculated. The star marks the image extraction coordinates of the feature corners, and the circle marks the re-projection image position of the feature corners, as shown in **Error! Reference source not found.**.
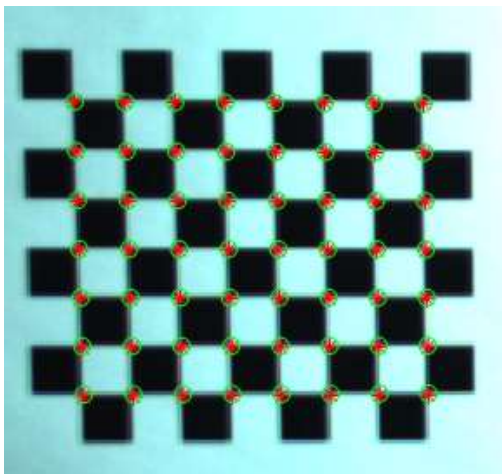
Figure 15. Image extraction and reproduction position of the corners

Figure 16 shows the error distribution between the image extraction and reprojection coordinates. The maximum error along the u-axis is 0.1736 pixels, and the maximum error along the v-axis is 0.9960 pixels. The average error along the u-axis was 0.0595 pixels, and the average error along the v-axis was 0.4634 pixels. Using the principle of

visual measurement, the maximum transformation range of the spatial position of the pixel is calculated.
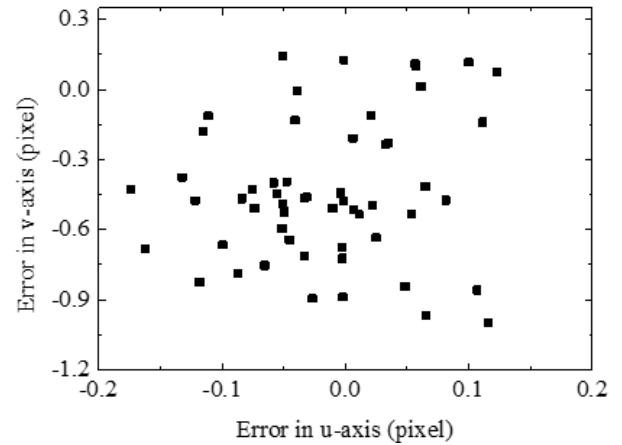
Figure 16. Reprojection error distribution of the corners.

The arbitrary point of the image has the above image coordinate error, which is the spatial position error caused by the image error after re-projection, as shown in Table 3.

Error in the rope image extraction

In the initial stage, when the flexible rope falls from the horizontal state, the rope has a low movement speed and the overall speed is uniform. The centerline extraction algorithm can be applied to extract the image of the flexible rope. The extraction effect is shown in Figure 17, and the centerline is superimposed on the original image. As the speed of the rope increases, the motion blur region generated by the image gradually increases in the fixed exposure period. Because of the uneven speed of the rope, it is not recommended to extract the results by the centerline algorithm in regions with a large speed at the end of the flexible rope, as shown in sections d and e

Table 3. Visual measurement error caused by the extrinsic matrix calculated using corners

Error along x-axis (mm)		Error along y-axis (mm)	
Average	Maximum	Aerage	Maximum

0.0807	0.2186	0.4557	0.9808
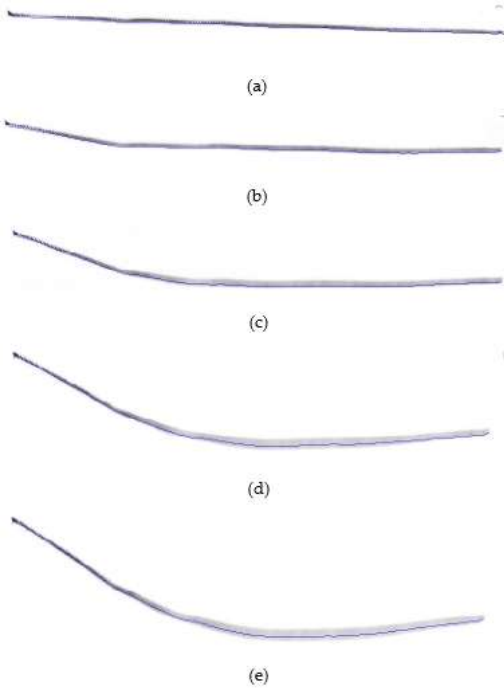
Figure 17. Image extraction result of the flexible rope using the centerline extraction method: (a) 1st frame image;(b) 5th frame image;(c) 9th frame image;(d) 13th frame image;(e) 15th frame image.

As shown in Figure 18, in order to avoid incorrect extraction of the centerline of the end region, the motion blur image segmentation algorithm is used to extract the rope image in the stage of fast speed, Because the movement speed of the rope and the grayscale of the motion-blurred area are not uniform, there will be interference in the motion-blurred region of the actual image after edge detection, as shown in part b.
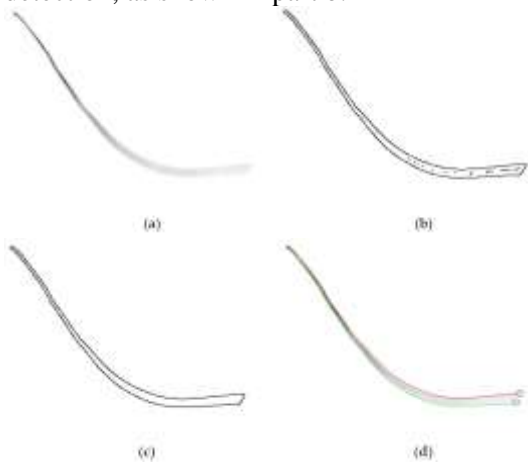

Figure 18. Flexible rope image extraction by motion blur segmentation algorithm: (a) Original image;(b) Edge detection image;(c) Edge image without noise;(d) Motion blur segmentation result.

The length of the interference fringe in the motion blur region is short and disconnected; therefore, the interference can be removed by retaining the largest connected domain in the edge image. The rope edge image refreshed the interference (shown in part c). The closed single-pixel rope edge can be divided into two moments of rope shape using the motion blur segmentation algorithm (shown in part d). The rope at the initial exposure and the final exposure can be extracted from the image, and the circle marked in Fig. 18 is the endpoint of the image of the two ropes. This method can avoid incorrect positioning of the centerline extraction algorithm in the motion blur area.

To verify the accuracy of the motion blur segmentation algorithm for the segmentation point, 200 frames of rope motion images were selected, and the edge image set of the rope was obtained by image preprocessing. The correct segmentation points are selected as the reference standard in the edge image set by artificial marking and then compared with the segmentation points extracted by the proposed algorithm to verify the accuracy. Figure 19 shows the position error of the endpoints at the initial and final exposures. Table 3 shows the error of the segmentation points between those extracted by the algorithm and the reference standard. It can be seen that at the end of the exposure, the detection error of the endpoint is great, but the average error of the four segmentation points extracted by the algorithm can be controlled within 2 pixels.
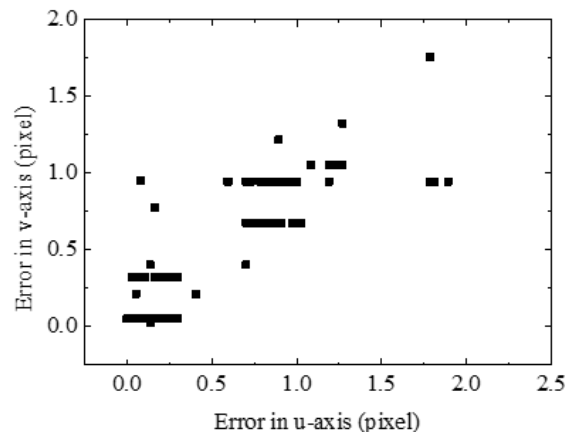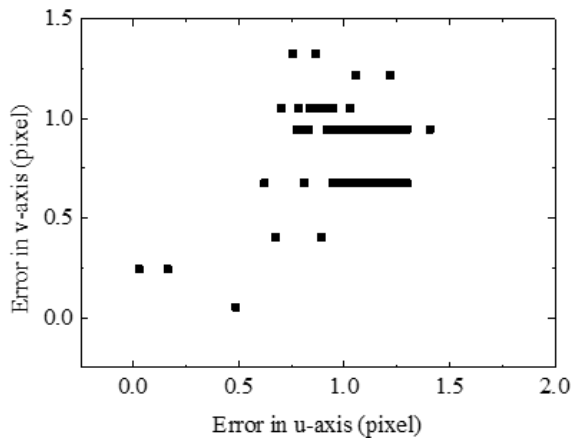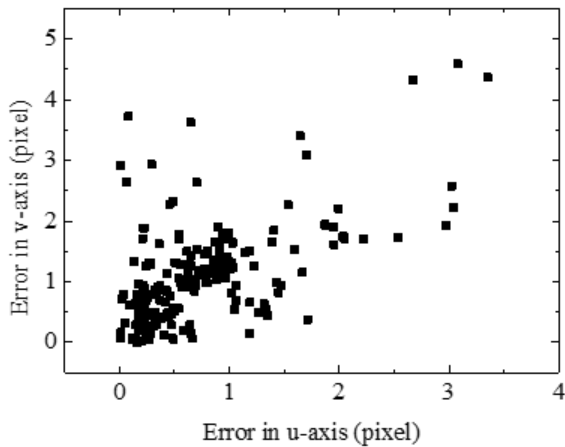

Figure 19.(a)
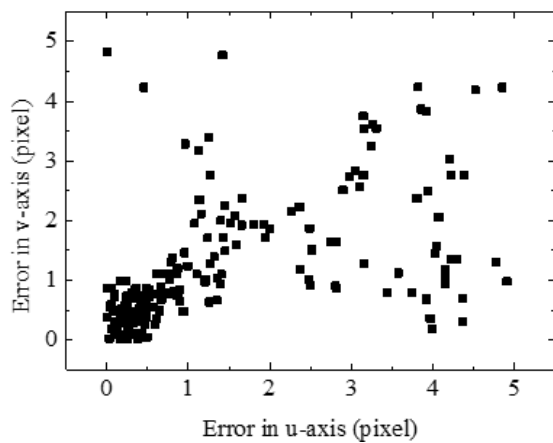
Figure 19.(b).

Figure 19.(c).

Figure 19.(d).
Figure 19. Segment point error distribution in the motion blur area: (a) Position error of the start point at the beginning of exposure;(b) Position error of the endpoint at the beginning of exposure;(c) Position error of the start point at the end of the exposure;(d) Position error of the endpoint at the end of the exposure

Table 4. Error statistics of segment points in the motion blur area.

Segmentation point	Average error (pixel)	Maximum error (pixel)
start point at the beginning of the exposure	0.8708	4.9825
start point at the end of the exposure	1.3870	5.5254
endpoint at the beginning of exposure	1.4109	1.7232
the endpoint at the end of the exposure	1.9651	6.4363

The maximum transformation range of the spatial pixel, when the image has the above image extraction error, is calculated as the spatial position error caused by the image extraction error, as shown in Table 4. The average error of the algorithm can be controlled within 2.5 mm under a measurement distance of 1.5 m.

Table 5. Space position errors of segment points caused by image extraction errors.

Segmentation point	Average error(pixel)	Maximum error(pixel)
start point at the beginning of the exposure	1.1034	6.3153
start point at the end of the exposure	1.7576	7.0036
endpoint at the beginning of exposure	1.7879	2.1796
the endpoint at the end of the exposure	2.4903	8.1586

Conclusions

In this study, we address the challenges posed by the non-uniform motion characteristics of ropes in aerospace applications. We propose an innovative edge segmentation operator designed specifically for the motion-blurred regions of ropes. Flexible ropes often present uniform grayscale and inconspicuous image characteristics, making them challenging to analyze visually. To overcome this, we introduce a novel visual material point-tracking algorithm tailored to accommodate rope bending and longitudinal elastic deformation.

Research limitations:

Simulation experiments validate the effectiveness of our motion blur segmentation algorithm. It successfully extracts the rope's configuration at the initial and end of an exposure, leading to improved accuracy with longer exposure times. This capability is crucial in aerospace scenarios where precise motion tracking of flexible elements like ropes is essential.

Recommendations for future research:

In the context of visual rope measurement experiments, we conduct a comprehensive analysis of various sources of error. These include errors originating from the visual measurement system, inaccuracies in image extraction, and spatial positioning errors resulting from image extraction failures.

Our research culminates in the verification of both the motion blur segmentation algorithm and the cable dynamics model based on the absolute node coordinate method. We carry out these verifications using a visual measurement system, acknowledging the presence of certain inherent errors. This work contributes to advancing the state-of-the-art in aerospace applications, where accurate measurement and modeling of flexible ropes play a critical role.

To comprehensively evaluate the advantages of novelties, additional work should be done regarding the comparison analysis with existing technologies. This involves integrating findings from the literature to provide a broader context for assessing the efficacy and practical implications of the proposed methodologies in aerospace applications.

References

[1] Shuguang M, Tianshu W. An Efficient Model of Tethers for Tethered Satellite Systems[J]. Advances in Astronautics Science and Technology, 2018, 1(2): 153–160.

[2] Razzaghi P, Al Khatib E, Bakhtiari S. Sliding mode and SDRE control laws on a tethered satellite system to de-orbit space debris[J]. Advances in Space Research, 2019, 64(1): 18–27.

[3] Mengali G, Quarta A A, Janhunen P. Electric Sail Performance Analysis[J]. Journal of Spacecraft & Rockets, 2008, 45(1): 122–129.

[4] Quarta A A, Mengali G, Janhunen P. Optimal interplanetary rendezvous combining electric sail and high thrust propulsion system[J]. Acta Astronautica, 2011, 68(5–6): 603–621.

[5] Bischof B. ROGER-Robotic geostationary orbit restorer[C]//54th International Astronautical Congress of the International Astronautical Federation, the International Academy of Astronautics, and the International Institute of Space Law. 2003: IAA–5.

[6] Huang P, Cai J, Meng Z, et al. Novel method of monocular real-time feature point tracking for tethered space robots[J]. Journal of Aerospace Engineering, 2013, 27(6): 04014039.

[7] Jin D, Wen H, Hu H. Modeling, dynamics and control of cable system [J]. Advances In Mechanics, 2004, 34(3): 304–313.

[8] Shabana A A. Definition of the Slopes and the Finite Element Absolute Nodal Coordinate Formulation[J]. Multibody System Dynamics, 1997, 1(3): 339–348.

[9] Shabana A A. Definition of ANCF Finite Elements[J]. Journal of Computational & Nonlinear Dynamics, 2015, 10.(۵)

[10] Shabana A A, Yakoub R Y. Three Dimensional Absolute Nodal Coordinate Formulation for Beam Elements: Theory[J]. Journal of Mechanical Design, 2001, 123(4): 614–621.

[11] Gerstmayr J, Shabana A A. Analysis of Thin Beams and Cables Using the Absolute Nodal Coordinate Formulation[J]. Nonlinear Dynamics, 2006, 45(1–2): 109–130.

[12] Zhu D, Lu Y, Tang J. Application of large deformation cable-beam element in multibody dynamic frame [C]//2007 Proceedings of the national symposium on structural dynamics. 2007.

[13] Dombrowski S V. Analysis of Large Flexible Body Deformation in Multibody Systems Using Absolute Coordinates[J]. Multibody System Dynamics, 2002, 8(4): 409–432.

[14] Liu C, Tian Q, Hu H. New spatial curved beam and cylindrical shell elements of gradient-deficient Absolute Nodal Coordinate Formulation[J]. Nonlinear Dynamics, 2012, 70(3): 1903–1918.

[15] Dmitrochenko O, Mikkola A. Digital Nomenclature Code for Topology and Kinematics of Finite Elements Based on the Absolute Nodal Co-Ordinate Formulation[J]. Proceedings of the Institution of Mechanical Engineers, Part K: Journal of Multi-body Dynamics, 2011, 225(1): 34–51.

[16] Zhang Y, Zhao Y, Tan C. The strain coupling problem of ANCF cable-beam element is decoupled from the model [J]. Chinese Journal of Theoretical and Applied Mechanics, 2016, 48(6): 1406–1415.

[17] Zhang Y, Wei C, Zhao Y. Modeling and simulation of relaxation rope dynamics based on ANCF [J]. Acta Aeronautica et Astronautica Sinica, 2017, 38(4): 157–165.

[18] Čepon G, Manin L, Boltežar M. Introduction of damping into the flexible multibody belt-drive model: A numerical and experimental investigation[J]. Journal of Sound & Vibration, 2009, 324(1–2): 283–296.

[19] Sauter Daniel. Modeling the Dynamic Characteristics of Slack Wire Cables in STOCKBRIDGE Dampers[D]. Technische Universität, 2004.

[20] Yamashita H, Matsutani Y, Sugiyama H. Longitudinal Tire Dynamics Model for Transient Braking Analysis: ANCF-LuGre Tire Model[J]. Journal of Computational & Nonlinear Dynamics, 2015, 10.(۳)

[21] Irvine H M. The Linear Theory of Free Vibrations of Suspended Membranes[J]. Proceedings of the Royal Society of London, 1976, 350(1662): 317–334.

[22] Angrilli F, Baglioni P, Bianchini G, et al. Multiple degree-of-freedom tracking for attitude control of an experimental system on tether-stabilized platform[C]//Acquisition, Tracking, and Pointing V. International Society for Optics and Photonics, 1991, 1482: 26–40.

[23] Yoo W S, Lee J H, Park S J, et al. Large Oscillations of a Thin Cantilever Beam: Physical Experiments and Simulation Using the Absolute Nodal Coordinate Formulation[J]. Nonlinear Dynamics, 2003, 34(1–2): 3–29.

[24] Yoo W S, Lee J H, Park S J, et al. Large Deflection Analysis of a Thin Plate: Computer Simulations and Experiments[J]. Multibody System Dynamics, 2004, 11(2): 185–208.

[25] Yoo W S, Lee J H, Park S J, et al. Large Deflection Analysis of a Thin Plate: Computer Simulations and Experiments[J]. Multibody System Dynamics, 2004, 11(2): 185–208.

[26] Jung S P, Park T W, Chung W S. Dynamic analysis of rubber-like material using absolute nodal coordinate formulation based on the non-linear constitutive law[J]. Nonlinear Dynamics, 2011, 63(1–2): 149–157.

[27] Kawaguti K, Terumichi Y, Takehara S, et al. The Study of the Tether Motion with Time-Varying Length Using the Absolute Nodal Coordinate Formulation with Multiple Nonlinear Time Scales[J]. 2007, 1(3): 491–500.

[28] Kim S-W, Kim N-S. Dynamic characteristics of suspension bridge hanger cables using digital image processing[J]. NDT & E International, 2013, 59: 25–33.

[29] Dong C Z, Ye X W, Jin T. Identification of structural dynamic characteristics based on machine vision technology[J]. Measurement, 2018, 126: 405–416.

[30] Luo L, Feng M Q, Wu Z Y. Robust vision sensor for multi-point displacement monitoring of bridges in the field[J]. Engineering Structures, 2018, 163: 255–266.

[31] Domae Y, Okuda H, Takauji H, et al. 3-dimensional measurement of cable configuration being based on feature tracking motion stereo[C]//Optomechatronic Systems Control III. International Society for Optics and Photonics, 2007, 6719: 67190J.

[32] Wang X, Liu J, Ning R, The invention relates to a spatial posture measurement method of motion cable based on binocular vision technology [J]. Optical Technique, 2010(05): 725–729.

[33] Liu J, Wang X, Zhang T. Binocular vision based flexible cable motion detection method and error analysis. [J]. Transactions of Beijing Institute of Technology, 2012(08): 795–800.

[34] E W, Wei C, Tan C, Zhang D, Zhao Y. Application of visual material point tracking in the verification of flexible cable model [J]. Acta Aeronautica et Astronautica Sinica, 2017,38(12):203-213.

COPYRIGHTS

HOW TO CITE THIS ARTICLE:

MohammadHassan Pachenari, "*Advancing Flexible Rope Motion Measurement in Aerospace: Vision-Based Innovations for Enhanced Accuracy and Efficiency through Edge Segmentation*", Journal of Aerospace Science and Technology, Vol 17, No2,2024, pp, 1-15
DOI: doi.org/10.22034/jast.2024.418390.1161
URL: https://jast.ias.ir/article_190191.html